Aberrant GPX4 processing reveals its critical roles in maintaining ROS homeostasis in *Citrus*

Barry, Shannon[1,2], Wang, Xin[2], & Wang, Nian[1,2]

[1] Citrus Research and Education Center, Institute of Food and Agricultural Sciences, University of Florida, Lake Alfred, FL 33850, U.S.A.

[2] Department of Microbiology and Cell Science, Institute of Food and Agricultural Sciences, University of Florida, Gainesville, FL 32611. U.S.A.

Corresponding author: nianwang@ufl.edu

Abstract

Glutathione peroxidases (GPXs) are widely recognized as key antioxidants that mitigate oxidative stress by detoxifying reactive oxygen species (ROS). However, GPXs are largely uncharacterized in citrus. Here, we demonstrated that *Citrus sinensis* contains four GPX proteins (CsGPX1–4). Unexpectedly, overexpression of *CsGPX4*, a homolog of *AtGPX8* in *Arabidopsis*, in citrus resulted in typical oxidative stress phenotypes including severe growth inhibition, chlorosis, and elevated intracellular ROS accumulation. Transmission electron microscopy (TEM) analysis further revealed stress responses at cellular level. Whole genome shot gun sequencing analysis showed that T-DNA insertion occurs in the UTR of *SWEET2* gene, which is unlikely to be responsible for the oxidative stress phenotypes. Immunoblotting revealed that CsGPX4 accumulates as a truncated protein in citrus, in contrast to the full-length version expressed in *Nicotiana benthamiana*. MALDI-TOF assays further confirmed the truncation of CsGPX4 in the transgenic line with the predicted cleavage site between L115-K117. This truncation was associated with altered subcellular localization, shifting from cytoplasmic and nuclear distribution in *N. benthamiana* to membrane association in citrus. Proteomic profiling further indicated extensive reprogramming of pathways involved in detoxification, cytoskeletal stability, hormone signaling, and cell wall modification. Our data suggests that *de facto* overexpression of truncated CsGPX4 may have dominant-negative effects on proteins interacting with CsGPX4, thus interfering with their normal functions. In conclusion, our study demonstrates CsGPX4 as a critical regulator of redox homeostasis and ROS homeostasis in

citrus and reveals selective truncation of CsGPX4 as a unique proteolytic or regulatory strategies in such processes.

Keywords: Citrus sinensis, Overexpression, CsGPXs, CsGPX4, AtGPX8, AtGPXs, transient expression, proteomics, post-translational truncation, redox homeostasis, species-specific

Introduction

Pathogens, insects, and environmental stressors contribute significantly to global crop yield losses, posing an escalating threat to food security (Bailey-Serres et al., 2019; Lesk et al., 2016). As the world population is projected to approach 10 billion by 2050, agricultural productivity must increase by an estimated 60% to meet future food demands (FAO, 2019; Fedoroff, 2015). This challenge underscores the urgent need to understand plant stress responses and develop more resilient crop varieties. A common physiological consequence of both biotic and abiotic stress is the overaccumulation of reactive oxygen species (ROS), including superoxide anion ($O_2\cdot^-$), hydrogen peroxide (H_2O_2), singlet oxygen ($^1O_2$), and hydroxyl radicals ($\cdot OH$). These molecules, though generated as byproducts of core metabolic processes such as photosynthesis, respiration, and nitrogen assimilation, accumulate to cytotoxic levels under stress conditions (Mittler, 2017; Wang et al., 2023). While excessive ROS can damage nucleic acids, proteins, lipids, and membranes, they also function as key signaling molecules that regulate plant development, immunity, and acclimation responses (Suzuki et al., 2012; Mitter et al., 2022). Thus, maintaining redox homeostasis is essential for plant survival and adaptation under adverse conditions.

Plants have evolved a complex antioxidant defense system comprising enzymatic and non-enzymatic components to mitigate ROS accumulation. Major enzymatic scavengers include superoxide dismutase (SOD), catalase (CAT), ascorbate peroxidase (APX), glutathione peroxidase (GPX), glutathione reductase (GR), peroxiredoxins (PRXs), thioredoxins (TRXs), and dehydroascorbate reductase (DHAR), which operate across distinct subcellular compartments to fine-tune ROS levels and maintain cellular redox balance (Wang et al., 2023). Among these, GPXs are thiol-based peroxidases that detoxify peroxides by using either glutathione (GSH) or thioredoxins (Trx) as electron donors (Bela et al., 2015; You and Chan, 2015). Notably, plant GPXs differ from their animal counterparts in both structure and cofactor usage—plant GPXs use cysteine (Cys) as the active site residue and prefer Trx, whereas animal

60 GPXs use selenocysteine (SeCys) and primarily depend on GSH (Islam et al., 2015; Wang et al.,
61 2023). Functionally, GPXs play important roles in plant responses to abiotic stresses such as
62 drought, salinity, extreme temperatures, and oxidative conditions. For example, overexpression
63 of *GPX5* in *Salvia miltiorrhiza* improved drought tolerance (Zhang et al., 2019), while knockout
64 of *GPX3* in *Oryza sativa* resulted in excessive H_2O_2 accumulation (Passaia et al., 2013).

65 GPX8 in particular has been implicated in protecting nuclear DNA and other organelles from
66 oxidative stress in *Arabidopsis* (Gaber et al., 2012). Overexpression of *AtGPX8* enhanced
67 oxidative tolerance, whereas its loss impaired root development and reduced stress resilience.
68 However, in woody species such as *C. sinensis*, functional studies of *GPX* genes remain limited.
69 For instance, Faltin et al. (2010) attempted to overexpress a phospholipid hydroperoxide GPX
70 (PHGPx) in *C. sinensis* but were only successful after abolishing enzymatic activity, indicating
71 potential toxicity or instability under overexpression conditions. In *Nicotiana benthamiana*,
72 overexpression of GPX8 alleviated cadmium-induced oxidative stress and preserved
73 photosynthetic pigments (Peng et al., 2024), highlighting the context-dependent functions of
74 GPXs.

75 In this study, we initially aimed to overexpress *CsGPX4*, a homologue of *AtGPX8*, to mitigate
76 oxidative stress caused by *Candidatus* Liberibacter asiaticus (CLas), which causes citrus
77 Huanglongbing (HLB). CLas is known to cause ROS accumulation, which contributes to phloem
78 cell death and subsequent HLB symptoms (Ma et al., 2022). GPXs were reported to be involved
79 in preventing oxidant-induced programmed cell death (PCD) (Passaia et al., 2014).
80 Unexpectedly, CsGPX4 overexpression resulted in the accumulation of a post-translationally
81 truncated protein isoform specific to *C. sinensis*, but not in *N. benthamiana*. This truncation was
82 associated with increased H_2O_2 accumulation, altered subcellular localization, chlorosis,
83 dwarfism, and ultrastructural cellular abnormalities. To our knowledge, this is the first report of a
84 plant antioxidant enzyme undergoing species-specific post-translational truncation in response to
85 overexpression, leading to a distinct stress-related phenotype.

86 **Results**

87 **Identification of *GPX* genes in *C. sinensis***

88 To identify *GPX* genes in *C. sinensis*, we conducted BLAST search with the eight GPX proteins
89 in *Arabidopsis*. Only 4 *GPX* genes were identified in *C. sinensis* (hereafter *CsGPX1-4*) (**Fig. 1A,**

90 **Supplementary Table 1**). Three of the four *CsGPX* genes (*CsGPX1*, *CsGPX2*, and *CsGPX4*)
91 reside on chromosome 5, whereas *CsGPX3* is located on chromosome 4 (**Fig. 1B**). The close
92 proximity of *CsGPX2* and *CsGPX4* on chromosome 5 suggests a possible duplication event.

93 CsGPX proteins range from 170 to 245 amino acids, with a corresponding molecular weight of
94 19.3-27 kDa. CsGPX4 is the smallest GPX protein in *C. sinensis.* All CsGPXs have negative
95 GRAVY values which indicate hydrophilic characteristic consistent with GPX families in other
96 plant species (Khan et al., 2024). Interestingly, CsGPX4 displayed an acidic pI of 4.76, in
97 contract to the basic pI values of >7.9 observed in other CsGPX proteins. In addition, CsGPX1,
98 CsGPX2, CsGPX3, and CsGPX4 were predicted to localize in the endoplasmic reticulum (ER),
99 mitochondria, plastids and cytoplasm, respectively (**Supplementary Table 1**).

100 On average, the CsGPXs have approximately 50% to 75% similarity (**Fig. 1C**). Multiple
101 sequence alignment revealed conserved regions of CsGPX proteins including the three conserved
102 motifs in plants: VNAS[R/K/Q]CG, LAFPCNQF, and WNF(S/T)KF (Churin et al., 1999). The
103 catalytic tetrad (cysteine (C), glutamine (Q), tryptophan (W), and asparagine (N)) of GPX was
104 observed (Tosatto et al., 2008). The three conserved Cys residues in the active sites of plant
105 GPXs were also present in citrus GPXs (**Fig. 1D**). All the four CsGPX proteins contain a
106 conserved thioredoxin (TRX)-like fold (**Fig. 1E**), consistent with that plant GPXs prefer TRX
107 rather than glutathione as a reducing agent (Gaber et al., 2012). AlphaFold 3 structural
108 predictions further revealed a well-resolved catalytic core with high confidence of the CsGPX
109 proteins, while the N-terminal regions exhibited low confidence.

110 **Overexpression of *CsGPX4* in citrus leads to oxidative stress phenotypes**

111 CLas triggers ROS accumulations, which contributes to phloem cell death and subsequent HLB
112 symptoms (Ma et al., 2022). GPXs are known to play important roles in preventing oxidant-
113 induced programmed cell death (Passaia 2014). A previous study reported that transgenic
114 overexpressing *AtGPX8*, a homologue of *CsGPX4* in *Arabidopsis* (**Fig. 1A**), increases plant
115 tolerance to oxidative stress (Gaber et al., 2012). Here, we investigated whether overexpression
116 of *CsGPX4* in *C. sinensis* can inhibit oxidative stress triggered by CLas. Specifically, CsGPX4
117 shares 79% identity and 90% similarity with AtGPX4 (**Fig. S1A**). The tertiary structures of
118 CsGPX4 and AtGPX8 predicated by Alphafold3 showed that they share a highly conserved TRX

119 fold (**Fig 1F; S1B**). Superimposition of these two models showed a root mean square deviation
120 (RMSD) of 0.364 Å, indicating a strong three-dimensional similarity (**Fig. S1B**).

121 We generated two stable *C. sinensis* lines overexpressing *CsGPX4* (GPX4-OX) driven by the
122 Cauliflower mosaic virus (CaMV) 35S promoter (**Fig. 2A, B**) via *Agrobacterium* mediated
123 transformation, which were identified by GFP fluorescence and further confirmed through
124 reverse transcription PCR (RT-PCR) (**Fig. 2D)**. Surprisingly, both GPX4-OX transgenic plants
125 exhibited oxidative stress phenotypes including chlorosis and reduced growth compared to
126 empty vector transformed controls (EV) (**Fig. 2B**). Transmission electron microscopy (TEM)
127 analysis revealed striking ultrastructural difference in midrib cells of CsGPX4-OX lines
128 compared with EV controls (**Fig. 3**). The EV control plant cells displayed typical healthy
129 architecture including compact cytoplasm, continuous membranes, and well-organized vacuoles.
130 In contrast, both CsGPX4-OX lines exhibited a progressive structural deterioration. At the
131 whole-cell level, CsGPX4-OX cells showed irregular cell boundaries and reduced cytoplasmic
132 density relative to the well-defined walls and dense cytoplasm of control plants (**Fig. 3A**).
133 Vacuolar morphology was also disrupted with CsGPX4-OX lines displaying clear deformities in
134 the tonoplast and intracellular membranes (**Fig. 3B**). Cytoplasmic organization was
135 compromised by the extensive vesiculation and disordered intracellular contents in CsGPX4-OX
136 (**Fig. 3C**). These abnormalities were accompanied by fragmentation of membrane systems, loss
137 of membrane continuity, and accumulation of electron dense materials, hallmarking of severe
138 cellular stress in CsGPX4-OX, but not in the EV control (**Fig. 3D**).

139 **CsGPX4 undergoes citrus-specific truncation and membrane-associated localization**

140 Previous studies demonstrate that overexpression of *AtGPX8* driven by the 35S promoter in
141 *Arabidopsis* (Gaber et al., 2012) and knockout of *AtGPX8* had no significant effects on plant
142 growth and development (Passaia et al., 2014). Because of the high similarity between AtGPX8
143 and CsGPX4, we anticipated that the abnormal phenotypes of GPX4-OX lines unlikely resulted
144 from overexpression of functional CsGPX4. Next, we examined whether GPX4-OX insertion
145 disrupts the gene function at the insertion site and whether the GPX4 protein was expressed as
146 expected.

147 Whole Genome Shot Gun Sequencing analysis identified the CsGPX4 T-DNA insertion site at
148 position chr2:1,646,389 in the *C. sinensis* genome, which was located within the 5′ untranslated

149 region (UTR) of the gene *SWEET2* (Cs_ont_2g002980.3) (**Fig. S2**). Since mutation of *SWEET2*
150 has no negative effects in growth or development of plants (Chen et al., 2015), it is unlikely that
151 the abnormal phenotypes of the CsGPX4-OX line resulted from insertion in the UTR of
152 *SWEET2*.

153 Next, we investigated the CsGPX4 expression in the CsGPX4-OX lines. Immunoblotting with an
154 anti-HA antibody confirmed expression of the tagged CsGPX4 protein in two independent
155 GPX4-OX lines (**Fig. 2C**). However, the observed protein band in the transgenic lines
156 corresponded to a molecular weight of approximately 11 kDa, significantly lower than the
157 predicted 22.6 kDa including 3HA tag (**Fig. 2C**). PCR amplification using cDNA as template
158 revealed the expected 505 bp fragment in both EV and GPX4-OX lines (**Fig. 2D**). Sequencing of
159 the amplified fragment eliminated the possibility of mutation of *CsGPX4* in the GPX4-OX lines
160 (**Fig. S3**).

161 To investigate the reasons underlying the truncated CsGPX4 (**Fig. 2C**), we transiently expressed
162 *CsGPX4* in *C. sinensis* and *Nicotiana benthamiana* (**Fig. S4A**). Immunoblot analysis of
163 transiently expressed CsGPX4 in *C. sinensis* detected the truncated CsGPX4 (**Fig. 4A**) similar to
164 transgenic expression (**Fig. 2E**), whereas a full length CsGPX4 of approximately 22.6 kDa
165 including the 3HA tag was observed in *N. benthamiana* (**Fig. 4A; S5**). This result confirmed the
166 integrity of CsGPX4 overexpression construct and suggested overexpression of CsGPX4 could
167 undergo a citrus specific truncation, but not in *N. benthamiana*.

168 To further confirm the truncation of CsGPX4 in the CsGPX4-OX transgenic plants, Matrix-
169 Assisted Laser Desorption/Ionization - Time-Of-Flight Mass Spectrometry (MALDI-TOF MS)
170 was performed. MALDI-TOF analysis of CsGPX4 purified through immunoprecipitation from
171 the CsGPX4-overexpressing *C. sinensis* line identified two major HA-tagged protein isoforms
172 with the m/z of 10,148.260 and 10,654.116, respectively (**Fig. 4B**), neither corresponding to the
173 predicted full-length CsGPX4-3HA (22.6 kDa). Based on the MALDI-TOF results, the predicted
174 cleavage window for the overexpressed CsGPX4-3HA was calculated to be between L115-K117.

175 Additionally, we transiently expressed CsGPX4-mVenus in *C. sinensis* and *N. benthamiana*
176 fused with Monomeric Venus *(*mVenus*)* (**Fig. S4B**) to determine if there are any differences in
177 the subcellular localization (**Fig. 4C**). Confocal microscopy analysis of CsGPX4-mVenus
178 showed a diffuse cytoplasmic and nuclear distribution in *N. benthamiana* leaf cells (**Fig. 4C;**

179 **S6**), which is consistent with the subcellular localization of AtGPX8 (Gaber et al., 2012). In
180 contrast, CsGPX4 in *C. sinensis* displayed a strong membrane-association. It is probable that
181 truncation affects the subcellular localization of CsGPX4.

182 **CsGPX4 overexpression disrupts intracellular redox homeostasis and reprograms the**
183 **proteome**

184 Because the CsGPX4-OX lines showed oxidative stress phenotypes, we quantified ROS
185 accumulation (**Fig. 5A-B**). H2DCFDA fluorescence revealed a significant elevation of
186 intracellular ROS in CsGPX4-OX leaves relative to EV controls ($p < 0.05$) (**Fig. 5A**). In contrast,
187 the extracellular H_2O_2 measured via the potassium iodide (KI) assay showed no significant
188 difference between OX-GPX4 leaves and EV lines (**Fig. 5B**).

189 To assess the broader physiological impact of CsGPX4-OX, we performed a global proteomic
190 profiling of leaves of CsGPX4-OX lines comparison to EV transformed plants (**Fig. 5C**). We
191 identified 150 downregulated proteins and 91 upregulated proteins that were significantly
192 regulated in CsGPX4-OX compared with EV. There were 16 GO biological processes that were
193 downregulated and two GO biological processes that were upregulated. Downregulated
194 PANTHER pathways were enriched for developmental pathways, including root and shoot
195 system development, broader multicellular organism and anatomical structure developmental
196 processes (**Fig. S7**). Upregulated PANTHER pathways were enriched for metabolic and
197 biosynthetic pathways (**Fig. S7**).

198 The significant results were associated with growth, cytoskeletal organization, hormone
199 signaling and redox detoxification including N-myristoyltransferase 1 (NMT1;
200 Cs_ont_1g019730.1), glutathione S-transferase U7 (GSTU7; Cs_ont_9g010810.1), microtubule-
201 associated protein 65 (MAP65; Cs_ont_0419670.1), transport inhibitor response 1 (TIR1;
202 Cs_ont_2g00600.1), UDP-glycosyltransferase 74E2 (UGT74E2; Cs_ont8g025420.1), and
203 sucrose synthase 4 (SUS4; Cs_ont_9g001770.2). The upregulated proteins included SNF1-
204 Related Protein Kinase 2.4 (SnRK2.4; Cs_ont_1g021000.1), and beta-D-xylosidase 2 (BXL2;
205 Cs_ont_9g001770.2).

206 **Discussion**

207 In this study, we performed systematic characterization of *C. sinensis* GPX family, comprising
208 *CsGPX1–CsGPX4*. Previous studies demonstrated that *Arabidopsis* contains eight GPX genes
209 (Rodriguez Milla et al. 2003), and tobacco has 14 *GPX* genes (Peng et al. 2024). GPXs play
210 important roles in detoxification of ROS in different compartments. For instance, GPXs were
211 reported to function in chloroplasts, cytosol, endoplasmic reticulum (ER), mitochondria, nucleus
212 and membrane (Attacha et al., 2017; Ferro et al. 2003, Rodriguez Milla et al. 2003, Jean-Benoit
213 et al. 2004; Chang et al. 2009; Gaber et al., 2012). Despite the small amount of GPXs in citrus,
214 citrus GPXs were predicted or observed to function in most of the known GPX locations
215 including ER, mitochondrion, plastid, cytosol and nucleus. Nevertheless, it is intriguing why
216 citrus contains so few GPX genes compared to other plant species.

217 Multiple studies showed that overexpression of *GPX8* increases plant tolerance against stresses
218 such as oxidative stress (Gaber 2012; Peng et al. 2024). Unexpectedly, overexpression of
219 *CsGPX4*, a homologue of *AtGPX8*, leads to phenotypes commonly associated with oxidative
220 stress, including growth inhibition, chlorosis, elevated ROS levels, and widespread cellular
221 disruption (Savchenko and Tikhonov, 2021). It is unlikely that the abnormal phenotypes are due
222 to overexpression of functional CsGPX4, interfere with the detoxification enzyme activity of
223 CsGPX4 or disruption of the gene function of insertion site. Overexpression of *GPX8* in
224 *Arabidopsis* and tobacco as well as mutation of *GPX8* has no negative effect on plant shoot
225 growth and development and does not cause oxidative stress phenotypes (Gaber 2012; Peng et al.
226 2024). In *Salvia miltiorrhiza*, overexpression of *GPX5* enhanced drought and oxidative stress
227 tolerance without causing negative effects on plant growth and development (Zhang et al., 2018).
228 Likewise, overexpression of *TaGPX3.2A* and *TaGPX3.4A* in wheat under salt and drought stress
229 enhanced ROS scavenging capacity (Jiang et al., 2023). WGS analysis showed that T-DNA
230 insertion occurs in the UTR of *SWEET2* gene. Prior studies indicate that *SWEET2* knockout
231 mutants in *A. thaliana* do not exhibit significant phenotypic alterations under normal growth
232 conditions (Chen et al., 2015). Instead, the oxidative stress phenotypes likely result from that
233 overexpression of *CsGPX4* causes truncation as evidenced by Western blotting and MALDI-
234 TOF analyses. Overexpression of truncated proteins in plants frequently results in dominant-
235 negative effects, where the truncated protein disrupts the function of the full-length proteins
236 including itself or interacting proteins. For instance, overexpression of truncated ERECTA
237 protein in *Arabidopsis* disrupts signalling of the whole ERECTA gene family and leads to

238 reduced vegetative growth (Villagarcia et al., 2012). GPX proteins are known to interact with
239 other proteins and have signaling functions (Delaunay et al., 2002; Miao et al., 2006). It is
240 probable that the overexpressed truncated CsGPX4 can still interact with other proteins, thus
241 interfering with their normal functions. Such disruptive effects were not observed in the *AtGPX8*
242 mutant, suggesting other protein(s) can complement its function. In addition, we could not
243 exclude other possibilities since the truncated CsGPX4 seems to locate to the membrane instead
244 of cytosol and nucleus of the full size CsGPX4 and its homologue AtGPX8 (Gaber et al., 2012).

245 Proteomic profiling revealed downregulation of key proteins involved in detoxification and
246 cellular structure, including NMT1, GSTU7, MAP65, TIR1, UGT74E2, and SUS4, and
247 upregulation of SnRK2.4 and BXL2, linking CsGPX4 overexpression misregulation to impaired
248 antioxidant defense, cytoskeletal destabilization, and altered hormone and cell wall signaling.
249 Specifically, NMT1 is essential for post-translational lipid modification; its knockout causes
250 severe growth arrest post-germination (Pierre et al., 2007). GSTU7 is involved in detoxifying
251 ROS and enhancing stress resilience (Ugalde et al., 2021). MAP65 facilitates microtubule
252 bundling and axial cell expansion (Lucas et al., 2011). TIR1 is a core auxin receptor; loss of
253 function impairs hormone-mediated growth (Ruegger et al., 1998). UGT74E2 modulates
254 oxidative stress response and water stress tolerance (Tognetti et al., 2010). Lastly, SUS4 is a key
255 to sucrose metabolism and cell wall biosynthesis in citrus (Wang et al., 2018). On the other hand,
256 upregulated proteins in CsGPX4-OX include several stress-response regulators. For instance,
257 SnRK2.4 is known to mediate ROS signaling, antioxidant gene expression (e.g., catalase,
258 ascorbate), and salt stress tolerance (Szymańska et al., 2019; Fujii & Zhu, 2009). These changes
259 in CsGPX4-OX plants indicate a disruption in core metabolic pathways as observed in oxidative
260 stress response (Savchenko and Tikhonov 2021), likely contributing to the observed growth
261 inhibition, microtubule instability, and reduced redox buffering in CsGPX4-OX plants.

262 In conclusion, our study identifies CsGPX4 as a critical regulator of redox balance in citrus
263 based on the analysis of the overexpression of truncated CsGPX4 and the consequences (**Fig. 6**).
264 How overexpression of *CsGPX4* leads to its truncation in citrus but not in tobacco remains to be
265 explored. The selective truncation of CsGPX4 underscores a unique proteolytic or regulatory
266 strategies related to redox signaling and ROS homeostasis.

267 **Materials and Methods**

268 **Computational analysis of GPX orthologs**

269 GPX homologs were identified from the *Arabidopsis* TAIR database
270 (https://www.arabidopsis.org/) and searched against the *Citrus sinensis* genome via BLAST
271 using the Citrus Genome Database (https://www.citrusgenomedb.org/). Full-length GPX
272 sequences from Arabidopsis, Citrus, and an outgroup were aligned using MAFFT (Katoh et al.,
273 2019) and trimmed with Gblocks on NGPhylogeny.fr (Talavera & Castresana, 2007; Castresana,
274 2000). Maximum likelihood trees were constructed in MEGA 12 (Kumar et al., 2024) with 1,000
275 bootstrap replicates. Jalview (Troshin et al., 2011) was used for alignment visualization.

276 GPX proteins were domain searched using NCBI Conserved Domain Database (CDD)
277 (Marchler-Bauer et al., 2015). Identified GPX proteins were chromosome-mapped using MG2C
278 (Chao et al., 2021). Multiple sequence alignments were performed with MUSCLE (Edgar, 2004)
279 and visualized in Jalview. Protein structure predictions for *C. sinensis* GPXs and AtGPX8 were
280 performed using AlphaFold 3 (Jumper et al., 2021; Varadi et al., 2022), with confidence
281 visualized via pLDDT scores.

282 **Vector construction**

283 The coding sequence of *CsGPX4* was amplified from *C. sinensis* cDNA using primers
284 incorporating XbaI and KpnI restriction sites (**Supplementary Table 2**). The PCR product was
285 gel-purified using the Monarch DNA Gel Extraction Kit and cloned into the binary vector
286 RCsVMV-erGFP-pCAMBIA-1380N-35S-BXKES (**Fig. 2A**), previously digested with XbaI and
287 KpnI (New England Biolabs), using the In-Fusion cloning system (Takara Bio). The resulting
288 construct included a C-terminal 3HA tag and GFP under control of the CaMV 35S promoter.

289 The constructs pCAMBIA1300S-35S-L279 (**Fig. S4A**) for transient expression
290 of *CsGPX4* and *AtGPX8* (Wang et al., 2017) and pCAMBIA1380-35S-mVenus (**Fig. S4B**) for
291 subcellular localization of *CsGPX4* were similarly assembled, but SacI was used for digestion
292 (**Supplementary Table 2**). Constructs were verified by Sanger sequencing.

293 **Plant transformation**

294 *A. tumefaciens* strain EHA105 carrying binary constructs was cultured to OD600 = 0.4–0.5 in
295 MS liquid medium (pH 5.4). *C. sinensis* seeds were surface-sterilized with 50% sodium
296 hypochlorite, plated on Murashige and Skoog (MS) medium, and kept in darkness for 6–8

297 weeks. Epicotyl segments were excised, immersed in *Agrobacterium*-containing medium for 20
298 min, dried on sterile filter paper, and transferred to co-cultivation medium containing 6-
299 Benzylaminopurine (BA), Indole-3-acetic acid (IAA), 2,4-Dichlorophenoxyacetic acid (2,4-D),
300 and acetosyringone. After three days in darkness, explants were transferred to selection medium
301 with kanamycin and timentin and maintained in darkness for four weeks. Emerging GFP-positive
302 shoots were micrografted onto Carrizo rootstock and transferred to MS medium supplemented
303 with IAA and IBA. Upon establishment, plants were moved to soil and acclimatized in growth
304 chambers.

305 **Agroinfiltration assay**

306 *C. sinensis* and *N. benthamiana* leaves were infiltrated using the strain *A. tumefaciens* EHA105
307 strain. *A. tumefaciens* carrying the plasmid was suspended in 10 mM $MgCl_2$, 10 mM 2-N-
308 morpholino ethanesulfonic acid potassium salt (MES-K), pH 5.6 with 100 µM of acetosyringone.
309 OD600 of 0.6 was obtained and mixed with *A. tumefaciens* carry vector pCAMBIA1300S-P19 in
310 a 1:1 ratio. Roughly six-week-old *N. benthamiana* was inoculated and kept in Plant Growth
311 Chambers from Geneva Scientific (#E-36HO Williams Bay, Wisconsin, United States). The
312 plants were grown at 23°C under high humidity in 16 h light/8 h dark and leaves were collected
313 two days later (Acanda et al., 2021). *C. sinensis* leaves were inoculated in a climate controlled
314 cool greenhouse with dim lighting.

315 **Confocal localization analysis**

316 Leaves were imaged for EGFP fluorescence using Confocal Laser Scanning Microscopy TCS-
317 SP5 from Leica (Mannheim, Germany, Europe). Samples were excited with 488 nm and detected
318 using photomultiplier tubes (PMT) tuned to 493-540 nm for EGFP.

319 **Western blot analysis**

320 *C. sinensis* and *N. benthamiana* leaves were collected and placed in liquid nitrogen and
321 TissueLyser II (Cat. #85300) from Qiagen (Hilden, Germany, Europe) was used to homogenize
322 the plant tissue. Total protein was extracted using CelLyticTM P Cell Lysis Reagent (#C2360)
323 and 1x Protease Inhibitor Cocktail (#P9599) from Sigma (Kawaski, Japan). Lysates were
324 centrifuged at 11,000 g for 15 minutes at 4°C. Supernatant was taken out and process was
325 repeated two more times. Laemmli Sample Buffer (#1610747) from Bio-Rad (Hercules, CA,

326 United States) with 10% of Beta-mercaptoethanol (βME) was mixed with lysates in 1:3 and
327 boiled at 99°C for 10 minutes. The denatured proteins of CsGPX4, AtGPX8 and EV were
328 separated using a 12% sodium dodecyl sulfate polyacrylamide gel electrophoresis gel (SDS-
329 PAGE). Immunoblots were washed in Tris Buffered Saline with Tween 20 (TBST) with 5%
330 Bovine serum albumin (BSA). Antibody used in this study was Anti-HA High Affinity
331 (#11867423001) from Roche (Basal, Switzerland, Europe). To visualize the immunoblots,
332 SuperSignalTM West Pico PLUS Chemiluminescent Substrate (#34580) from Thermo Fisher
333 was used. Loading was confirmed by Ponceau S staining (#P7170) from Sigma-Aldrich (St.
334 Louis, Missouri, United States) of the Rubisco large subunit (RbcL), which served as a total
335 protein loading control.

336 **TEM analysis**

337 Small leaf sections were collected and fixed in cold 3% Gluteraldehyde in 0.1M Sorensen's
338 Phosphate buffer (SPBS), pH 6.8 for 24 hours. Tissues were then rinsed three times for 30
339 minutes in 0.1M Sorensen's Phosphate Buffer. Tissues were Osmicated in 1% osmium tetroxide
340 for four hours room temperature. Tissues were then rinsed 3 times for one hour each in 0.1M
341 SPBS. Tissues were dehydrated in acetone of concentrations 25%, 50%, 90% 100%, 100%,
342 100% for 20 minutes. Tissues were infiltrated in a 1:1 mixture of acetone wrapped in plastic
343 overnight at RT. Infiltrated tissues were made in a 1:3 mixture of acetone and infiltrated again
344 for six hours. Tissues were transferred to embedded molds, oriented and sat in RT until settled.
345 The polymerize plastic was heated at 60°C for 12 hours.

346 The embedded tissue was placed on Epoxy resin blocks that were provided from University of
347 Florida Interdisciplinary Center Electron Microscopy (ICBR-EM) Core for ultramicrotomy and
348 TEM examination. Tissues were made into semi-thick resin sections and collected onto super
349 frost plus glass slides from Fisher Scientific (#22-037-246) and stained with toluidine blue.
350 Ultrathin resin sections of 100 nm were collected on carbon coated Formvar 2x1 mm nickle slot
351 grids-TB from Electron Microscopy Sciences (EMS) (Hatfield, PA, United States). Ultrathin
352 resin sections were treated with 1% meta periodate for 15 minutes and washed with H_2O. Tissues
353 were air dried and then post-stained with 2% aqueous uranyl acetate and citrate from EMS.
354 Sections were then examined with a Field Electron and Ion (FEI) Teecnai G2 Spirit Twin TEM

355 (Hillsboro, OR, United States) and Digital Micrograph Software Gatan (Pleasanton, CA, United
356 States).

357 **H_2O_2 quantification**

358 Extracellular H_2O_2 concentrations were measured based on Kumar et al., (2011). Samples were
359 adjusted to fit on 96-well plate. Infiltrated *C. sinensis* tissues were weighed and grinded and 1:4
360 of 0.1% (w/v) of trichloroacetic acid (TCA) and 5 µL of samples or standard was mixed with
361 28.25 µL of 1.0 phosphate buffer at a pH of 7.0 and 16.25 µL of 1.0 potassium iodide (KI)
362 solution. Plates were incubated in room temperature in the dark for five minutes. Absorbance of
363 290 nm was measured for the oxidized product. H_2O_2 concentrations were then calculated using
364 the standard curve with H_2O_2 concentration and fresh weight measured in µmol/g.

365 For H_2DCFDA Fluorescence Intensity, H_2DCFDA stained was used from *C. sinensis* infiltrated
366 with the following protocol with minor adjustments (Kaur et al., 2016) and manufactures
367 instructions from Invitrogen (Eugene, OR, United States). Leaf size of 25 mm^2 were collected
368 and cleaned using distilled H_2O and incubated in 10 µM H2DCFDA from Thermo Fisher
369 (#D399) and were vacuum infiltrated for five minutes. Samples were washed using distilled
370 H_2O. Fresh PBS, pH 7.2 was added and incubated in the dark for 30 minutes. Fluorescence was
371 measured using BMG LABTECH VANTAstar (Ortenberg, Germany) at Ex/Em= 485/535 nm in
372 end point mode and analysis was performed and RFU was calculated (Aimonen et al., 2022).

373 **mRNA expression analysis by RT-qPCR**

374 Total RNA was extracted using RNeasy Plant Mini Kit (Cat. #74904) following manufacturer's
375 instructions. QScript cDNA Supermix (#95048-025) from Quantabio (Beverly, MA, United
376 States) was used to synthesize cDNA. cDNA was diluted 10 times for RT-qPCR and reactions
377 were carried out using 1 µL of cDNA, 1 µL of specific primers (**Supplementary Table. 2**), 7 µL
378 of H_2O, and 10 uL of Thermo-Fisher Scientific Fast SYBR Green Master Mix (Cat. #4385617).
379 RT-qPCR was conducted using 95°C for 20s followed by 40 cycles at 95°C for 1s, and 60°C for
380 20s. Relative gene expression was calculated for fold change using the $2^{-\Delta\Delta C_T}$ method (Livak &
381 Schmittgen, 2001). *CsFBOX* (encoding a F-Box family) was used as the endogenous
382 housekeeping control (Mafra et al, 2012)

383 **Whole-genome sequencing and T-DNA insertion site identification**

384 To identify the genomic insertion site of the CsGPX4 overexpression construct, whole-genome
385 resequencing was performed using genomic DNA extracted from a transgenic plant line.
386 Genomic DNA was extracted using the Promega Genomic DNA Kit (#A1120, Madison, WI,
387 USA) and paired-end libraries were prepared and sequenced on the Illumina platform to generate
388 150 bp paired-end reads. Raw sequencing reads were assessed for quality using FastQC, and
389 adapters were removed using Trimmomatic. High-quality reads were aligned to the *C. sinensis*
390 genome (Zhong et al., 2024) concatenated with the full CsGPX4 T-DNA plasmid sequence using
391 BWA-MEM. SAM files were converted to BAM, sorted, and indexed using SAMtools.

392 To determine the T-DNA insertion site, read pairs mapping partially to the T-DNA plasmid and
393 partially to the *C. sinensis* genome were identified. Integrative Genomics Viewer (IGV) was
394 used to visualize junction reads, soft-clipping events, and mate-pair connections (Thorvaldsdottir
395 et al., 2013). BEDTools was used to intersect candidate insertion coordinates with the *C. sinensis*
396 genome annotation in GFF3 format to assess gene disruption.

397 **Shotgun proteomics**

398 Infiltrated *C. sinensis* leaves were collected and placed in liquid nitrogen and using the
399 TissueLyser II to homogenize. Total protein was extracted using 50 mM Tris-HCL, pH 8.0,
400 0.01% n-dodecyl- β-maltoside (DDM), and 1x of Plant Proteaserrest Protease Inhibitor Cocktail
401 (#786) from G-BioSciences (St. Louis, MO, United States). Lysis preparation consists of
402 centrifuging sample at 4°C for 15 minutes and removing supernatant. This process was repeated
403 3 times. Laemmli sample buffer (#1610747) was mixed with lysates in 1:3 and boiled at 99°C for
404 10 minutes. An 12% SDS-PAGE gel was made with 50 µg of lysis protein loaded with three
405 biological replicates of CsGPX4 and EV and was run very briefly. Each lane was excised for in-
406 gel trypsin digestion. Trypsin (#V5280) from Promega (Madison, WI, United States) was used
407 for digestion. The peptides were desalted using Pierce C18 Spin Tips & Columns (#87784) from
408 Thermo Fisher following manufacturer's manual and samples were analyzed using a Thermo
409 Orbitrap Exploris 240 combined Vanquish Neo UHPLC with a 120-minute LC gradient (Jiang et
410 al, 2025). Mass spectrometry data were acquired in data-dependent acquisition (DDA) mode.
411 Full MS scans (MS1) were collected over an m/z range of 375-1475 at a resolution of 120,000.
412 MS/MS fragmentation was performed at a resolution of 15,000, targeting the most abundant
413 precursor ions within a 3-second duty cycle. The normalized AGC target is set to 300% for MS1,

414 and a standard MS2 AGC target was applied using a normalized HCD collision energy of 30%.
415 Dynamic exclusion was enabled with a 45-second exclusion duration. PatternLab V was used for
416 data analysis with extracted ion chromatograms for protein expression profiles (Santos et a.,
417 2022). Protein expression changes were evaluated using extracted-ion chromatograms
418 (XIC). Briefly, two-sample Student's t-test was used for differential analysis with p cutoff being
419 0.05. To control false discovery rate, Banjamini-Hochberg FDR estimator was included in
420 the TFold module. F-stringency, L-stringency and q-value were set to 0.1, 0, and 0.05 as
421 default settings. Minimal absolute fold change for proteins with significance was 1.7.

422 **MALDI-TOF MS assay**

423 Total protein was processed as stated in Shotgun Proteomics section. Pierce™ Anti-HA Agarose
424 (#26181) from Thermo Fisher was used for immunoprecipitation. Lysates were incubated
425 rotating with Anti-HA Agarose slurry at 4°C for four hours. Reaction was washed using 50 mM
426 Tris-HCL, pH 8.0. Proteins were eluted using 0.1M Glycine, pH 2.0 and 1:10 1M
427 Monoammonium Phosphate (ABC). C18 Spin Tips & Columns (#87784) from Thermo Fisher
428 was applied for desalting following manufacturer's instructions. Protein at 50 µL was
429 concentrated at 10 uM.

430 For Matrix-assisted laser desorption/ionization time-of flight (MALDI-TOF), 1 µL aliquot of
431 purified protein was mixed 1:1 with saturated sinapinic acid (SA) matrix prepared in 70% CAN
432 and 0.1% TFA. A 1 µL aliquot of this mixture was spotted onto a stainless steel MALDI target
433 plate and air dried. Spectra were acquired on a Bruker autoflex maX MALDI-TOF (Billerica,
434 Massachusetts, United States) mass spectrometer operating in linear positive ion mode over an
435 m/z range of 5,000-22,000. Spectra were acquired using FlexControl and analyzed with
436 PolyTools 2.0. Signal intensities were reported in arbitrary units (a.u.) scales $x10^4$.

437

438 **Acknowledgements**

439 We thank Dr. Karen Kelley at University of Florida Interdisciplinary Center for Biotechnology
440 Research for TEM expertise and Dr. Kari Basso for running our sample into the MALDI-TOF.
441 Additionally, we would like to thank Dr. Zhonglin Mou for providing us the vector for transient
442 expression. We would like to thank our funding sources of the Emergency Citrus Disease

443 Research and Extension Program grants 2022-70029-38471 and 2021-67013-34588 and the U.S.
444 Department of Agriculture's National Institute of Food and Agriculture grant 2023-70029-
445 41280. MALDI-TOF funding was provided from NIH grant award numbers S10 OD021758-
446 01A1 and S10 OD030250-01A1.

447 **Author Contributions**

448 S.B. and N.W. conceived the work and drafted manuscript. S.B. also designed and preformed
449 experiments. X.W. ran the CsGPX4 and EV samples in LC-MS for global proteomics.

450 **Completing interests**

451 All authors declare no conflict of interest and competing financial interest.

452 **Data Availability**

453 Whole genome resequencing data for CsGPX4 were deposited to NCBI under project ID
454 (PRJNA1419271). Global proteomic data of CsGPX4 and EV are deposited in MassIVE
455 repository (MSV000100757) and ProteomeXchange Consortium (PXD074185) (Vizcaino et al.,
456 2015).

457

458

459

460 **References**

461 1. Abramson, J., Adler, J., Dunger, J., Evans, R., Green, T., Pritzel, A., Ronneberger, O.,
462 Willmore, L., Ballard, A. J., Bambrick, J., Bodenstein, S. W., Evans, D. A., Hung, C. C.,
463 O'Neill, M., Reiman, D., Tunyasuvunakool, K., Wu, Z., Žemgulytė, A., Arvaniti, E.,
464 Beattie, C., … Jumper, J. M. (2024). Accurate structure prediction of biomolecular
465 interactions with AlphaFold 3. Nature, 630(8016), 493–500.
466 https://doi.org/10.1038/s41586-024-07487-w

467 2. Aimonen, K., Imani, M., Hartikainen, M., Suhonen, S., Vanhala, E., Moreno, C., Rojas,
468 O. J., Norppa, H., & Catalán, J. (2022). Surface functionalization and size modulate the
469 formation of reactive oxygen species and genotoxic effects of cellulose
470 nanofibrils. Particle and fibre toxicology, 19(1), 19. https://doi.org/10.1186/s12989-022-
471 00460-3

472 3. Bailey-Serres, J., Parker, J. E., Ainsworth, E. A., Oldroyd, G. E., & Schroeder, J. I.
473 (2019). Genetic strategies for improving crop yields. Nature, 575(7781), 109–118.

474 4. Bela, K., Horváth, E., Gallé, Á., Szabados, L., Tari, I., & Csiszár, J. (2015). Plant
475 glutathione peroxidases: emerging role of the antioxidant enzymes in plant development
476 and stress responses. Journal of Plant Physiology, 176, 192–201.

477 5. Bela, K., Riyazuddin, R., & Csiszár, J. (2022). Plant glutathione peroxidases: non-heme
478 peroxidases with large functional flexibility as a core component of ROS-processing
479 mechanisms and signalling. Antioxidants (Basel, Switzerland), 11(8), 1624.
480 https://doi.org/10.3390/antiox11081624

481 6. Bové, J. M. (2006). Huanglongbing: a destructive, newly-emerging, century-old disease
482 of citrus. Journal of Plant Pathology, 7–37.

483 7. Cao, S., Hepowit, N., & Maupin-Furlow, J. A. (2015). Ubiquitin-Like Protein SAMP1
484 and JAMM/MPN+ Metalloprotease HvJAMM1 constitute a system for reversible
485 regulation of metabolic enzyme activity in Archaea. PloS One, 10(5), e0128399.
486 https://doi.org/10.1371/journal.pone.0128399

487 8. Castresana, J. (2000). Selection of Conserved Blocks from Multiple Alignments for Their
488 Use in Phylogenetic Analysis. Molecular Biology and Evolution, 17(4), 540–
489 552. https://doi.org/10.1093/oxfordjournals.molbev.a026334

490 9. Chae, H. B., Bae, S. B., Paeng, S. K., Wi, S. D., Phan, K. A. T., Kim, M. G., Kim, W. Y.,
491 Yun, D. J., & Lee, S. Y. (2023). The physiological role of thiol-based redox sensors in
492 plant defense signaling. The New phytologist, 239(4), 1203–1211.
493 https://doi.org/10.1111/nph.19018

494 10. Chao, J., Li, Z., Sun, Y., Aluko, O. O., Wu, X., Wang, Q., & Liu, G. (2021). MG2C: a
495 user-friendly online tool for drawing genetic maps. Molecular horticulture, 1(1), 16.
496 https://doi.org/10.1186/s43897-021-00020-x

497 11. Chen, H. Y., Huh, J. H., Yu, Y. C., Ho, L. H., Chen, L. Q., Tholl, D., Frommer, W. B., &
498 Guo, W. J. (2015). The Arabidopsis vacuolar sugar transporter SWEET2 limits carbon
499 sequestration from roots and restricts Pythium infection. The Plant journal : for cell and
500 molecular biology, 83(6), 1046–1058. https://doi.org/10.1111/tpj.12948

501 12. Churin, Y., Schilling, S., & Börner, T. (1999). A gene family encoding glutathione
502 peroxidase homologues in Hordeum vulgare (barley). *FEBS letters*, *459*(1), 33–38.
503 https://doi.org/10.1016/s0014-5793(99)01208-9

504 13. Dum, M. T., Teufel, F., Thumuluri, V., Armenteros, J. J. A., Johansen, A. R., Winther,
505 O., & Nielsen, H. (2024). DeepLoc 2.1: multi-label membrane protein type prediction
506 using protein language models. Nucleic Acids Research, 52(W1), W215–
507 W220. https://doi.org/10.1093/nar/gkae237

508 14. Ebel, R. C. (2017). Huanglongbing: Mechanism of citrus decline and horticulture
509 management in Florida. Integrated Plant Health Services, Fort Myers, FL, 17, 2019.
510 www.IPHSLLC.com

511 15. Edgar, R. C. (2004). MUSCLE: multiple sequence alignment with high accuracy and
512 high throughput. Nucleic Acids Research, 32(5), 1792–1797.
513 https://doi.org/10.1093/nar/gkh340

514 16. Estrella-Maldonado, H., González-Cruz, C., Matilde-Hernández, C., Adame-García, J.,
515 Santamaría, J. M., Santillán-Mendoza, R., & Flores-de la Rosa, F. R. (2023). Insights into

516 the molecular basis of Huanglongbing tolerance in Persian lime (Citrus latifolia Tan.)
517 through a transcriptomic approach. International Journal of Molecular Sciences, 24(8),
518 7497. https://doi.org/10.3390/ijms24087497

519 17. Faltin, Z., Holland, D., Velcheva, M., Tsapovetsky, M., Roeckel-Drevet, P., Handa, A.
520 K., Abu-Abied, M., Friedman-Einat, M., Eshdat, Y., & Perl, A. (2010). Glutathione
521 peroxidase regulation of reactive oxygen species level is crucial for in vitro plant
522 differentiation. Plant & cell physiology, 51(7), 1151–1162.
523 https://doi.org/10.1093/pcp/pcq082

524 18. FAO. (2019). The State of Food and Agriculture 2019. Moving forward on food loss and
525 waste reduction. Rome. Licence: CC BY-NC-SA 3.0 IGO.

526 19. Fedoroff, N. V. (2015). Food in a future of 10 billion. Agriculture & Food Security, 4(1),
527 11.

528 20. Fujii, H., & Zhu, J. K. (2009). Arabidopsis mutant deficient in 3 abscisic acid-activated
529 protein kinases reveals critical roles in growth, reproduction, and stress. Proceedings of
530 the National Academy of Sciences of the United States of America, 106(20), 8380–8385.
531 https://doi.org/10.1073/pnas.0903144106

532 21. Fujita, Y., Nakashima, K., Yoshida, T., Katagiri, T., Kidokoro, S., Kanamori, N.,
533 Umezawa, T., Fujita, M., Maruyama, K., Ishiyama, K., Kobayashi, M., Nakasone, S.,
534 Yamada, K., Ito, T., Shinozaki, K., & Yamaguchi-Shinozaki, K. (2009). Three SnRK2
535 protein kinases are the main positive regulators of abscisic acid signaling in response to
536 water stress in Arabidopsis. Plant & Cell Physiology, 50(12), 2123–2132.
537 https://doi.org/10.1093/pcp/pcp147

538 22. Gaber, A., Ogata, T., Maruta, T., Yoshimura, K., Tamoi, M., & Shigeoka, S. (2012). The
539 involvement of Arabidopsis glutathione peroxidase 8 in the suppression of oxidative
540 damage in the nucleus and cytosol. Plant & Cell Physiology, 53(9), 1596–1606.
541 https://doi.org/10.1093/pcp/pcs100

542 23. Gottwald, T. R., Da Graça, J. V., & Bassanezi, R. B. (2007). Citrus Huanglongbing: the
543 pathogen and its impact. Plant Health Progress, 8(1). https://doi.org/10.1094/php-2007-
544 0906-01-rv

24. Gutscher, M., Sobotta, M. C., Wabnitz, G. H., Ballikaya, S., Meyer, A. J., Samstag, Y., & Dick, T. P. (2009). Proximity-based protein thiol oxidation by H2O2-scavenging peroxidases. The Journal of biological chemistry, 284(46), 31532–31540. https://doi.org/10.1074/jbc.M109.059246

25. Herbette, S., Roeckel-Drevet, P., & Drevet, J. R. (2007). Seleno-independent glutathione peroxidases. More than simple antioxidant scavengers. The FEBS journal, 274(9), 2163–2180. https://doi.org/10.1111/j.1742-4658.2007.05774.

26. Holmgren, A., & Morgan, F. J. (1976). Enzyme reduction of disulfide bonds by thioredoxin. The reactivity of disulfide bonds in human choriogonadotropin and its subunits. *European journal of biochemistry*, *70*(2), 377–383. https://doi.org/10.1111/j.1432-1033.1976.tb11027.x

27. Iqbal, A., Yabuta, Y., Takeda, T., Nakano, Y., & Shigeoka, S. (2006). Hydroperoxide reduction by thioredoxin-specific glutathione peroxidase isoenzymes of Arabidopsis thaliana. The FEBS journal, 273(24), 5589–5597. https://doi.org/10.1111/j.1742-4658.2006.05548.x

28. Islam, T., Manna, M., & Reddy, M. K. (2015). Glutathione peroxidase of Pennisetum glaucum (PgGPx) is a functional Cd^{2+} dependent peroxiredoxin that enhances tolerance against salinity and drought stress. PLoS One, 10(11), e0143344.

29. Jiang, B., Su, C., Wang, Y., Xu, X., Li, Y., & Ma, D. (2023). Genome-wide identification of Glutathione peroxidase (GPX) family genes and silencing TaGPX3.2A reduced disease resistance in wheat. Plant physiology and biochemistry : PPB, 204, 108139. https://doi.org/10.1016/j.plaphy.2023.108139

30. Jiang, Z., Islam, K. N., Wolfe, M., O'Connell, M., Williams, D., Florance, A., Vinyard, D. J., Zhang, X., Brenner, M., Kiss, A. J., Liu, X., & Wang, X. (2025). Enhancing photosynthesis under salt stress via directed evolution in cyanobacteria. PLANT PHYSIOLOGY. https://doi.org/10.1093/plphys/kiaf209

31. Jumper, J., Evans, R., Pritzel, A., Green, T., Figurnov, M., Ronneberger, O., Tunyasuvunakool, K., Bates, R., Žídek, A., Potapenko, A., Bridgland, A., Meyer, C., Kohl, S. A. A., Ballard, A. J., Cowie, A., Romera-Paredes, B., Nikolov, S., Jain, R.,

574 Adler, J., Back, T., … Hassabis, D. (2021). Highly accurate protein structure prediction
575 with AlphaFold. Nature, 596(7873), 583–589. https://doi.org/10.1038/s41586-021-
576 03819-2

577 32. Kaur, N., Sharma, I., Kirat, K., & Pati, P. K. (2016). Detection of reactive oxygen species
578 in Oryza sativa L. (Rice). Bio-protocol, 6(24), e2061.
579 https://doi.org/10.21769/BioProtoc.2061

580 33. Khan, W. U., Khan, L. U., Khan, N. M., Wenquan, W., & Chen, F. (2024). Evolutionary
581 insights and expression dynamics of the glutathione peroxidase (GPX) gene family in
582 water lily (Nymphaea colorata) in response to multiple abiotic stresses. Plant Stress, 14,
583 100699. https://doi.org/10.1016/j.stress.2024.100699

584 34. Kumar, N., Ebel, R. C., & Roberts, P. D. (2011). Superoxide dismutase activity in
585 kumquat leaves infected with *Xanthomonas axonopodis* pv. citri. The Journal of
586 Horticultural Science and Biotechnology, 86(1), 62-68.

587 35. Kumar, S., Stecher, G., Suleski, M., Sanderford, M., Sharma, S., & Tamura, K. (2024).
588 MEGA12: Molecular Evolutionary Genetic Analysis Version 12 for Adaptive and Green
589 Computing. Molecular biology and evolution, 41(12), msae263.
590 https://doi.org/10.1093/molbev/msae263

591 36. Lesk, C., Rowhani, P., & Ramankutty, N. (2016). Influence of extreme weather disasters
592 on global crop production. Nature, 529(7584), 84–87.

593 37. Li, J., Li, L., Pang, Z., Kolbasov, V. G., Ehsani, R., Carter, E. W., & Wang, N. (2019).
594 Developing Citrus Huanglongbing (HLB) management strategies based on the severity of
595 symptoms in HLB-endemic citrus-producing regions. Phytopathology, 109(4), 582–592.
596 https://doi.org/10.1094/PHYTO-08-18-0287-R

597 38. Livak, K. J., & Schmittgen, T. D. (2001). Analysis of relative gene expression data using
598 real-time quantitative PCR and the 2(-Delta Delta C(T)) Method. Methods (San Diego,
599 Calif.), 25(4), 402–408. https://doi.org/10.1006/meth.2001.1262

600 39. Lucas, J. R., Courtney, S., Hassfurder, M., Dhingra, S., Bryant, A., & Shaw, S. L. (2011).
601 Microtubule-associated proteins MAP65-1 and MAP65-2 positively regulate axial cell

602 growth in etiolated Arabidopsis hypocotyls. The Plant Cell, 23(5), 1889–1903.
603 https://doi.org/10.1105/tpc.111.084970

604 40. Ma, W., Pang, Z., Huang, X., Xu, J., Pandey, S. S., Li, J., Achor, D. S., Vasconcelos, F.
605 N. C., Hendrich, C., Huang, Y., Wang, W., Lee, D., Stanton, D., & Wang, N. (2022).
606 Citrus Huanglongbing is a pathogen-triggered immune disease that can be mitigated with
607 antioxidants and gibberellin. Nature communications, 13(1), 529.
608 https://doi.org/10.1038/s41467-022-28189-9

609 41. Mafra, V., Kubo, K. S., Alves-Ferreira, M., Ribeiro-Alves, M., Stuart, R. M., Boava, L.
610 P., Rodrigues, C. M., & Machado, M. A. (2012). Reference Genes for Accurate
611 Transcript Normalization in Citrus Genotypes under Different Experimental
612 Conditions. PLoS ONE, 7(2), e31263. https://doi.org/10.1371/journal.pone.0031263

613 42. Marchler-Bauer, A., Derbyshire, M. K., Gonzales, N. R., Lu, S., Chitsaz, F., Geer, L. Y.,
614 Geer, R. C., He, J., Gwadz, M., Hurwitz, D. I., Lanczycki, C. J., Lu, F., Marchler, G. H.,
615 Song, J. S., Thanki, N., Wang, Z., Yamashita, R. A., Zhang, D., Zheng, C., & Bryant, S.
616 H. (2015). CDD: NCBI's conserved domain database. Nucleic Acids Research,
617 43(Database issue), D222–D226. https://doi.org/10.1093/nar/gku1221

618 43. Margis, R., Dunand, C., Teixeira, F. K., & Margis-Pinheiro, M. (2008). Glutathione
619 peroxidase family - an evolutionary overview. The FEBS journal, 275(15), 3959–3970.
620 https://doi.org/10.1111/j.1742-4658.2008.06542.x

621 44. Mittler R. (2017). ROS Are Good. Trends in plant science, 22(1), 11–19.
622 https://doi.org/10.1016/j.tplants.2016.08.002

623 45. Mittler, R., Zandalinas, S. I., Fichman, Y., & Van Breusegem, F. (2022). Reactive
624 oxygen species signalling in plant stress responses. *Nature reviews. Molecular cell*
625 *biology*, *23*(10), 663–679. https://doi.org/10.1038/s41580-022-00499-2

626 46. Morris, K., Linkies, A., Müller, K., Oracz, K., Wang, X., Lynn, J. R., Leubner-Metzger,
627 G., & Finch-Savage, W. E. (2011). Regulation of seed germination in the close
628 Arabidopsis relative Lepidium sativum: a global tissue-specific transcript analysis. Plant
629 Physiology, 155(4), 1851–1870. https://doi.org/10.1104/pp.110.169706

630 47. Navrot, N., Collin, V., Gualberto, J., Gelhaye, E., Hirasawa, M., Rey, P., Knaff, D. B.,
631 Issakidis, E., Jacquot, J. P., & Rouhier, N. (2006). Plant glutathione peroxidases are
632 functional peroxiredoxins distributed in several subcellular compartments and regulated
633 during biotic and abiotic stresses. Plant physiology, 142(4), 1364–1379.
634 https://doi.org/10.1104/pp.106.089458

635 48. Pan, J. L., & Bardwell, J. C. (2006). The origami of thioredoxin-like folds. Protein
636 Science, 15(10), 2217–2227. https://doi.org/10.1110/ps.062268106

637 49. Passaia, G., Queval, G., Bai, J., Margis-Pinheiro, M., & Foyer, C. H. (2014). The effects
638 of redox controls mediated by glutathione peroxidases on root architecture in Arabidopsis
639 thaliana. Journal of Experimental Botany, 65(5), 1403–1413.
640 https://doi.org/10.1093/jxb/ert486

641 50. Peng, X., Ma, T., Song, K., Ji, X., Xiang, L., Chen, N., Zu, R., Xu, W., Zhu, S., & Liu,
642 W. (2024). Overexpression of NtGPX8a improved cadmium accumulation and tolerance
643 in tobacco (Nicotiana tabacum L.). Genes, 15(3), 366.
644 https://doi.org/10.3390/genes15030366

645 51. Pierre, M., Traverso, J. A., Boisson, B., Domenichini, S., Bouchez, D., Giglione, C., &
646 Meinnel, T. (2007). N-myristoylation regulates the SnRK1 pathway in Arabidopsis. The
647 Plant Cell, 19(9), 2804–2821. https://doi.org/10.1105/tpc.107.051870

648 52. Qi, Y., & Grishin, N. V. (2005). Structural classification of thioredoxin-like fold proteins.
649 Proteins, 58(2), 376–388. https://doi.org/10.1002/prot.20329

650 53. Rodriguez Milla MA, Maurer A, Rodriguez Huete A, Gustafson JP. (2003) Glutathione
651 peroxidase genes in *Arabidopsis* are ubiquitous and regulated by abiotic stresses through
652 diverse signaling pathways. Plant J. 36(5):602-15. https://doi.org/10.1046/j.1365-
653 313x.2003.01901.x

654 54. Ruegger, M., Dewey, E., Gray, W. M., Hobbie, L., Turner, J., & Estelle, M. (1998). The
655 TIR1 protein of Arabidopsis functions in auxin response and is related to human SKP2
656 and yeast grr1p. Genes & Development, 12(2), 198–207.
657 https://doi.org/10.1101/gad.12.2.198

658 55. Savchenko, T., & Tikhonov, K. (2021). Oxidative Stress-Induced Alteration of Plant
659 Central Metabolism. *Life (Basel, Switzerland)*, *11*(4), 304.
660 https://doi.org/10.3390/life11040304

661 56. Suzuki, N., Koussevitzky, S., Mittler, R., & Miller, G. (2012). ROS and redox signalling
662 in the response of plants to abiotic stress. Plant, cell & environment, 35(2), 259–270.
663 https://doi.org/10.1111/j.1365-3040.2011.02336.x

664 57. Szymańska, K. P., Polkowska-Kowalczyk, L., Lichocka, M., Maszkowska, J., &
665 Dobrowolska, G. (2019). SNF1-Related Protein Kinases SnRK2.4 and SnRK2.10
666 Modulate ROS Homeostasis in Plant Response to Salt Stress. International journal of
667 molecular sciences, 20(1), 143. https://doi.org/10.3390/ijms20010143

668 58. Talavera, G., & Castresana, J. (2007). Improvement of phylogenies after removing
669 divergent and ambiguously aligned blocks from protein sequence alignments. Systematic
670 biology, 56(4), 564–577. https://doi.org/10.1080/10635150701472164

671 59. Tholey, A., & Becker, A. (2017). Top-down proteomics for the analysis of proteolytic
672 events - Methods, applications and perspectives. Biochimica et biophysica acta.
673 Molecular cell research, 1864(11 Pt B), 2191–2199.
674 https://doi.org/10.1016/j.bbamcr.2017.07.002

675 60. Thorvaldsdóttir, H., Robinson, J. T., & Mesirov, J. P. (2013). Integrative Genomics
676 Viewer (IGV): high-performance genomics data visualization and exploration. *Briefings*
677 *in bioinformatics*, *14*(2), 178–192. https://doi.org/10.1093/bib/bbs017

678 61. Tognetti, V. B., Van Aken, O., Morreel, K., Vandenbroucke, K., van de Cotte, B., De
679 Clercq, I., Chiwocha, S., Fenske, R., Prinsen, E., Boerjan, W., Genty, B., Stubbs, K. A.,
680 Inzé, D., & Van Breusegem, F. (2010). Perturbation of indole-3-butyric acid homeostasis
681 by the UDP-glucosyltransferase UGT74E2 modulates Arabidopsis architecture and water
682 stress tolerance. *The Plant cell*, *22*(8), 2660–2679.
683 https://doi.org/10.1105/tpc.109.071316

684 62. Tosatto, S. C., Bosello, V., Fogolari, F., Mauri, P., Roveri, A., Toppo, S., Flohé, L.,
685 Ursini, F., & Maiorino, M. (2008). The catalytic site of glutathione

686 peroxidases. Antioxidants & redox signaling, 10(9), 1515–1526.
687 https://doi.org/10.1089/ars.2008.2055

688 63. Troshin, P. V., Procter, J. B., & Barton, G. J. (2011). Java bioinformatics analysis web
689 services for multiple sequence alignment--JABAWS:MSA. Bioinformatics (Oxford,
690 England), 27(14), 2001–2002. https://doi.org/10.1093/bioinformatics/btr304

691 64. Ugalde, J. M., Lamig, L., Herrera-Vásquez, A., Fuchs, P., Homagk, M., Kopriva, S.,
692 Müller-Schüssele, S. J., Holuigue, L., & Meyer, A. J. (2021). A dual role for glutathione
693 transferase U7 in plant growth and protection from methyl viologen-induced oxidative
694 stress. Plant Physiology, 187(4), 2451–2468. https://doi.org/10.1093/plphys/kiab444

695 65. Varadi, M., Anyango, S., Deshpande, M., Nair, S., Natassia, C., Yordanova, G., Yuan,
696 D., Stroe, O., Wood, G., Laydon, A., Žídek, A., Green, T., Tunyasuvunakool, K.,
697 Petersen, S., Jumper, J., Clancy, E., Green, R., Vora, A., Lutfi, M., Figurnov, M., …
698 Velankar, S. (2022). AlphaFold Protein Structure Database: massively expanding the
699 structural coverage of protein-sequence space with high-accuracy models. Nucleic Acids
700 Research, 50(D1), D439–D444. https://doi.org/10.1093/nar/gkab1061

701 66. Villagarcia, H., Morin, A. C., Shpak, E. D., & Khodakovskaya, M. V. (2012).
702 Modification of tomato growth by expression of truncated ERECTA protein from
703 Arabidopsis thaliana. *Journal of experimental botany*, *63*(18), 6493–6504.
704 https://doi.org/10.1093/jxb/ers305

705 67. Vizcaíno, J. A., Csordas, A., del-Toro, N., Dianes, J. A., Griss, J., Lavidas, I., Mayer, G.,
706 Perez-Riverol, Y., Reisinger, F., Ternent, T., Xu, Q. W., Wang, R., & Hermjakob, H.
707 (2016). 2016 update of the PRIDE database and its related tools. *Nucleic acids*
708 *research*, *44*(D1), D447–D456. https://doi.org/10.1093/nar/gkv1145
709

710 68. Wang, C., Zhou, M., Zhang, X., Yao, J., Zhang, Y., & Mou, Z. (2017). A lectin receptor
711 kinase as a potential sensor for extracellular nicotinamide adenine dinucleotide
712 in *Arabidopsis thaliana*. *eLife*, *6*, e25474. https://doi.org/10.7554/eLife.25474

713 69. Wang, N., & Trivedi, P. (2013). Citrus huanglongbing: A newly relevant disease presents
714 unprecedented challenges. Phytopathology, 103(7), 652–665.

715 70. Wang, W., Cheng, Y., Ruan, M., Ye, Q., Yao, Z., Wang, R., Zhou, G., Liu, D., & Wan, H.
716 (2023). Comprehensive identification of glutathione peroxidase (GPX) gene family in

717 response to abiotic stress in pepper (Capsicum annuum L.). Gene, 881, 147625.
718 https://doi.org/10.1016/j.gene.2023.147625

719 71. Wang, X., Lin, L., Tang, Y., Xia, H., Zhang, X., Yue, M., Qiu, X., Xu, K., & Wang, Z.
720 (2018). Transcriptomic insights into citrus segment membrane's cell-wall components
721 relating to fruit sensory texture. BMC Genomics, 19(1), 280.
722 https://doi.org/10.1186/s12864-018-4669-y

723 72. Wu, G. A., Terol, J., Ibanez, V., López-García, A., Pérez-Román, E., Borredá, C.,
724 Domingo, C., Tadeo, F. R., Carbonell-Caballero, J., Alonso, R., Curk, F.,
725 Du, D., Ollitrault, P., Roose, M. L., Dopazo, J., Gmitter, F. G., Rokhsar, D. S., & Talon, M.
726 (2018). Genomics of the origin and evolution of Citrus. Nature, 554(7692), 311–316.
727 https://doi.org/10.1038/nature25447

728 73. Xiao, C., Zhang, H., Xie, F., Pan, Z. Y., Qiu, W. M., Tong, Z., Wang, Z. Q., He, X. J.,
729 Xu, Y. H., & Sun, Z. H. (2022). Evolution, gene expression, and protein–protein
730 interaction analyses identify candidate CBL-CIPK signalling networks implicated in
731 stress responses to cold and bacterial infection in citrus. BMC Plant Biology, 22(1), 420.
732 https://doi.org/10.1186/s12870-022-03809-0

733 74. You, J., & Chan, Z. (2015). ROS regulation during abiotic stress responses in crop plants.
734 Frontiers in Plant Science, 6, 1092.

735 75. Zhai, C. Z., Zhao, L., Yin, L. J., Chen, M., Wang, Q. Y., Li, L. C., Xu, Z. S., & Ma, Y. Z.
736 (2013). Two wheat glutathione peroxidase genes whose products are located in
737 chloroplasts improve salt and H_2O_2 tolerances in Arabidopsis. PLoS One, 8(10), e73989.
738 https://doi.org/10.1371/journal.pone.0073989

739 76. Zhang, L., Wu, M., Teng, Y., Jia, S., Yu, D., Wei, T., Chen, C., & Song, W. (2019).
740 Overexpression of the glutathione peroxidase 5 (RcGPX5) gene from Rhodiola crenulata
741 increases drought tolerance in Salvia miltiorrhiza. Frontiers in Plant Science, 9, 1950.
742 https://doi.org/10.3389/fpls.2018.01950

743 77. Zhang, M., Zi, Y., Yang, X., Yang, X., Zhu, L., Cai, H., Yin, T., Liu, X., & Zhang, H.
744 (2025). Genome-wide analysis of the CsAP2/ERF gene family of sweet orange (Citrus

745 sinensis) and joint analysis of transcriptional metabolism under salt stress. Annals of
746 botany, 135(6), 1165–1180. https://doi.org/10.1093/aob/mcaf006

747 78. Zhang, X., Li, X., Zhao, R., Zhou, Y., & Jiao, Y. (2020). Evolutionary strategies drive a
748 balance of the interacting gene products for the CBL and CIPK gene families. The New
749 Phytologist, 226(5), 1506–1516. https://doi.org/10.1111/nph.16445

750 79. Zhao, X., Qiao, L., & Wu, A. M. (2017). Effective extraction of Arabidopsis adherent
751 seed mucilage by ultrasonic treatment. Scientific Reports, 7(1), 40672.

752 80. Zhong, C., Yang, X., Niu, J., Zhou, X., Zhou, J., Pan, G., Sun, Z., Chen, J., Cao, K., &
753 Luan, M. (2024). Transcriptome analysis of *Citrus Aurantium* L. to study synephrine
754 biosynthesis during developmental stages. *PeerJ*, *12*, e17965.
755 https://doi.org/10.7717/peerj.17965

756

757 **Figure legends**

758 **Figure 1. Characterization of the CsGPX proteins in *C. sinensis*.** (**A**) Neighbor-Joining
759 phylogenetic tree of CsGPX and AtGPX proteins, constructed using MEGA-X with 1,000
760 bootstrap replicates. The bacterial protein SeBtuE was used as the outgroup. Cs: *C. sinensis*. At:
761 *Arabidopsis thaliana*. (**B**) Chromosomal positions of *CsGPX1-CsGPX4* in *C. sinensis*. Genomic
762 positions were obtained from the *C. sinensis* reference genome and visualized using custom
763 annotation scripts. (**C**) Pairwise amino acid identity analysis of CsGPX proteins. (**D**) Multiple
764 sequence alignment of CsGPX proteins generated with Clustal omega. The catalytic residues are
765 represented by black arrows. The three conserved motifs are highlighted by red boxes. The three
766 conserved Cys are marked by triangles. (**E**) Conserved domain analysis of CsGPX proteins.
767 TRX: Thioredoxin domain. Bar diagrams illustrate domain length and positions in each protein.
768 (**F**) Predicted tertiary structures of CsGPX proteins generated using AlphaFold3. All proteins
769 exhibit a well-resolved TRX fold in dark blue while N-terminal regions show intrinsically
770 disordered or flexible conformations (low confidence in orange).

771 **Figure 2. Verification of GPX4 overexpression and evidence of post-translational**
772 **truncation in transgenic *C. sinensis* lines. (A)** Schematic representation of plasmid construct
773 used for *CsGPX4* overexpression. LB and RB, the left and right borders of the T-DNA region;

774 CsVMV, the cassava vein mosaic virus promoter; GFP, green fluorescent protein; 35T, the
775 cauliflower mosaic virus 35S terminator; NosP and NosT, the nopaline synthase gene promoter
776 and its terminator; NptII, the coding sequence of neomycin phosphotransferase II. HA:
777 Hemagglutinin tag. (**B**) Phenotypic comparison of empty vector (EV) and *CsGPX4*
778 overexpression (OX-CsGPX4) *C. sinensis* plants. The picture was taken 1 year after planting in
779 soil. (**C**) Immunoblot detection of HA-tagged CsGPX4 using an anti-HA antibody. Rubisco was
780 used as a loading control. (**D**) Reverse transcription PCR confirmation of *CsGPX4* transgene
781 expression in the OX-CsGPX4 lines. cDNA synthesized from total RNA was amplified using
782 CsGPX4-specific primers. Amplicons of identical size were observed in both OX and EV plant,
783 confirming correct transcript expression. PCR products were resolved by agarose gel
784 electrophoresis.

785 **Figure 3. Transmission electron microscopy (TEM) analysis of *C. sinensis* leaves**
786 **overexpressing *CsGPX4*.** (**A**) Overall cell organization. CsGPX4-OX plant cells exhibit
787 irregular boundaries and reduced cytoplasmic density compared to the empty vector (EV)
788 transformed lines. (**B**) Vacuolar structure. CsGPX4-OX cells show pronounced tonoplast (green
789 arrow) and membrane (blue arrow) deformation compared to EV. (**C**) Cytoplasmic organization.
790 CsGPX4-OX cells display extensive vesiculation (arrow) and disorganization of intracellular
791 contents (dashed arrow) compared to EV. (**D**) Membrane integrity. OX lines show fragmented
792 membranes, loss of structural continuity, and accumulation of electron-dense material (arrow),
793 with more severe defects observed in OX-GPX4-2. Scale bars: (**A**) = 2 µm; (**B**) = 1 µm; (**C**) = 2
794 µm; (**D**) = 0.5 µm.

795 **Figure 4. Host specific processing and subcellular localization of CsGPX4 in *C. sinensis***
796 **and *N. benthamiana*.** (**A**) Immunoblot analysis of CsGPX4-3HA transiently expressed in *C.*
797 *sinensis* and *N. benthamiana.* A truncated 11 kDa protein was detected in *C. sinensis* and a full-
798 length protein of 22.5 kDa was detected in *N. benthamiana*. Rubisco was used as a loading
799 control. (**B**) MALDI-TOF analysis reveals truncated CsGPX4 proteoform in CsGPX4-OX lines.
800 MALDI-TOF mass spectrum of immunopurified CsGPX4 from citrus leaf tissues expressing
801 HA-tagged CsGPX4 ranging (m/z) 6000-22000. Two prominent peaks were observed at m/z
802 10,548.260 and 10,654.116. Both masses are substantially lower than the predicted full-length
803 protein (22.5 kDa). The 10,548.260 m/z peak dominates in intensity, suggesting this truncated
804 form is the most stable isoform. Intensity values are presented in arbitrary units (a.u.) scales at

805 x104. (**C**) Subcellular localization of CsGPX4 in *C. sinensis* and *N. benthamiana.* Confocal
806 microscopy of leaf epidermis expressing CsGPX4-EGFP-mVenus. Fluorescence displays a
807 strong membrane-associated pattern in *C. sinensis*. Fluorescence displays GPX4 localization in
808 cytoplasm and nucleus in *N. benthamiana*. Scale bars: *C. sinensis* = 25 µm; *N. benthamiana* = 50
809 µm.

810 **Figure 5. Quantification of ROS levels and proteomic analysis of the CsGPX4-OX lines and**
811 **wild type.** (**A**) Intracellular ROS levels measured using the fluorescent probe H2DCFDA. Three
812 biological replicates were used, $p < 0.05$, student's t test. (**B**) Quantification of extracellular H_2O_2
813 using the KI assays. Three biological replicates were used, $p < 0.05$, student's t test. (**C**) Volcano
814 plot showing differently expressed proteins in CsGPX4-OX leaves relative to EV controls.
815 Significantly downregulated proteins (red) labeled include NMT1, GSTU7, MAP65, TIR1,
816 UGT74E2, and SUS4. Significantly upregulated proteins (teal) labeled include SnRK2.4 and
817 BXL2. Non-significant proteins (gray). Three biological replicates were used.

818 **Figure 6. Proposed model of CsGPX4 metabolic shift results of some involved proteins and**
819 **CsGPX4 truncation affects before and after. Top:** Schematic summary illustrating the
820 contrasting roles of CsGPX4 in its functional (left) and truncated (right) states. Functional state
821 (green): Intact CsGPX4 supports reactive oxygen species (ROS) detoxification and redox
822 balance, sustaining cytoskeletal organization (MAP6, NMT1), hormonal signaling (UGT42E,
823 SnRK2.4), and balanced carbohydrate metabolism (SUSA, BXL2). These processes maintain
824 healthy cytoplasmic structure, intact organelles, and thickened cell walls. Truncated state (red):
825 Loss of full-length CsGPX4 compromises peroxidase activity, leading to ROS accumulation and
826 downregulation of redox-related and cytoskeletal proteins (GSTU7, MAP6, NMT1, SUSA).
827 Stress-associated proteins (SnRK2.4, BXL2) become upregulated, promoting vacuolization,
828 organelle swelling, and cell wall degradation.

829

830

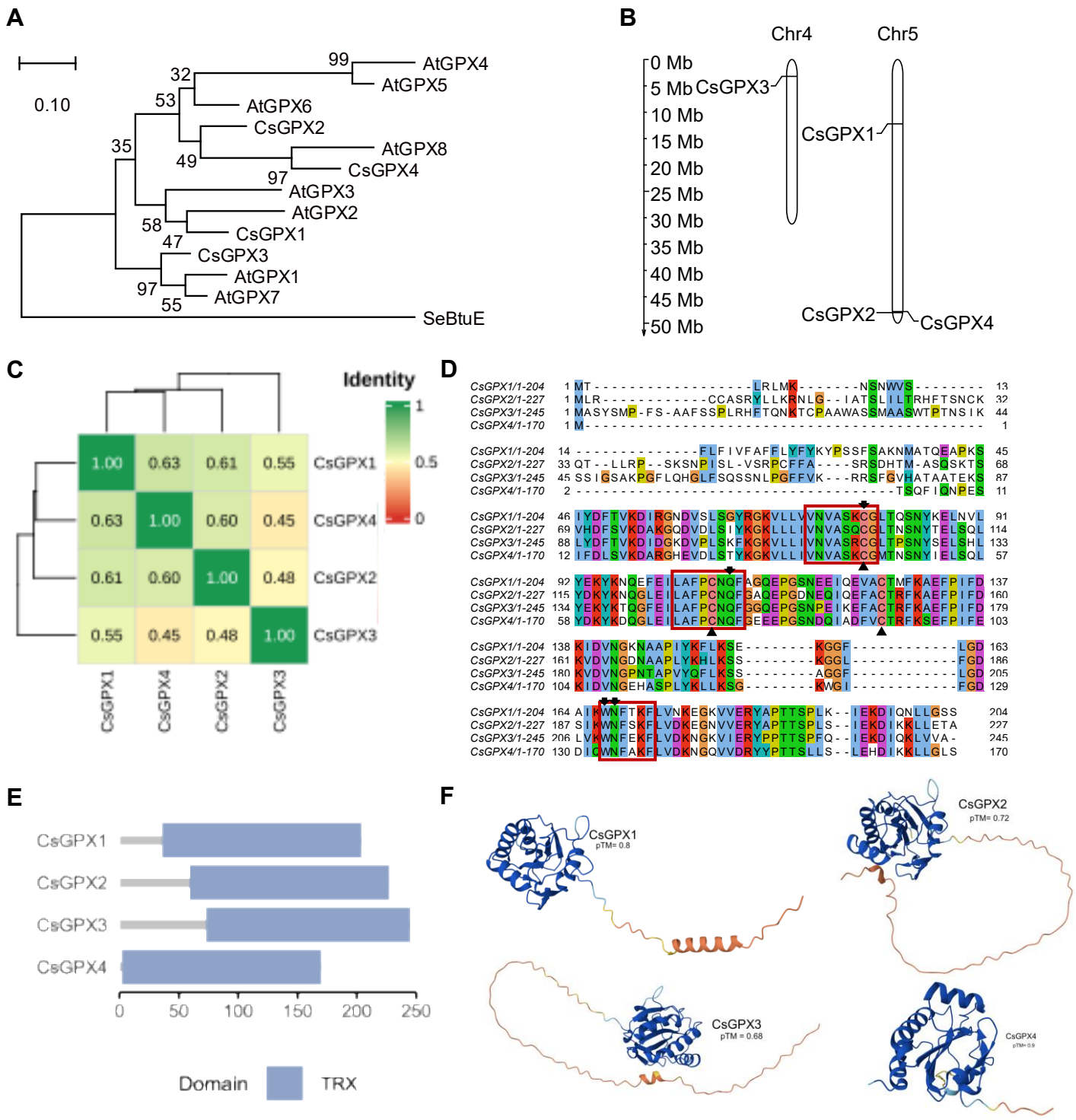

Figure 1. Characterization of the CsGPX proteins in *C. sinensis*. (**A**) Neighbor-Joining phylogenetic tree of CsGPX and AtGPX proteins, constructed using MEGA-X with 1,000 bootstrap replicates. The bacterial protein SeBtuE was used as the outgroup. Cs: *C. sinensis*. At: *Arabidopsis thaliana*. (**B**) Chromosomal positions of *CsGPX1-CsGPX4* in *C. sinensis*. Genomic positions were obtained from the *C. sinensis* reference genome and visualized using custom annotation scripts. (**C**) Pairwise amino acid identity analysis of CsGPX proteins. (**D**) Multiple sequence alignment of CsGPX proteins generated with Clustal omega. The catalytic residues are represented by black arrows. The three conserved motifs are highlighted by red boxes. The three conserved Cys are marked by triangles. (**E**) Conserved domain analysis of CsGPX proteins. TRX: Thioredoxin domain. Bar diagrams illustrate domain length and positions in each protein. (**F**) Predicted tertiary structures of CsGPX proteins generated using AlphaFold3. All proteins exhibit a well-resolved TRX fold in dark blue while N-terminal regions show intrinsically disordered or flexible conformations (low confidence in orange).

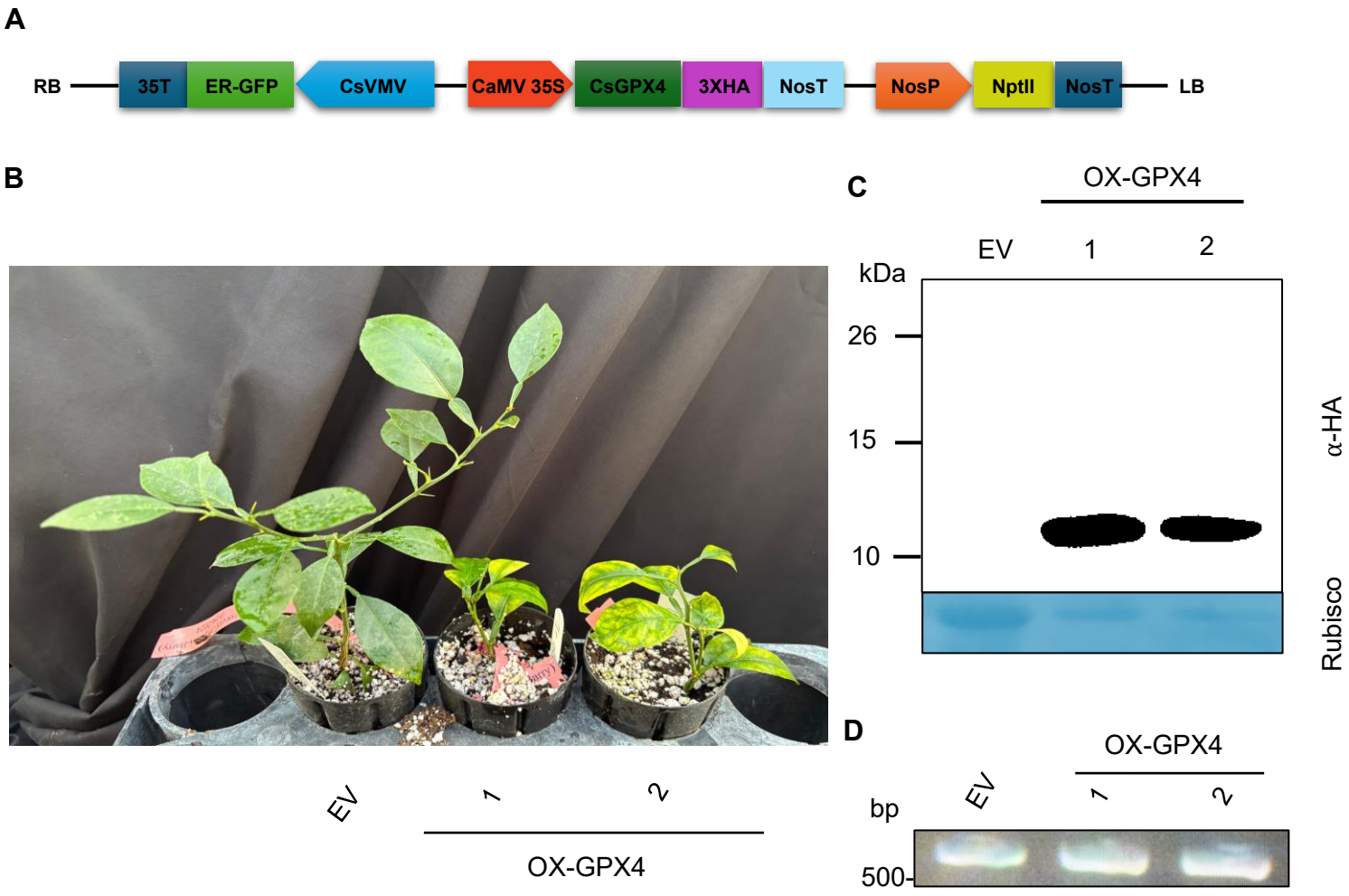

Figure 2. Verification of GPX4 overexpression and evidence of post-translational truncation in transgenic *C. sinensis* lines. (A) Schematic representation of plasmid construct used for *CsGPX4* overexpression. LB and RB, the left and right borders of the T-DNA region; CsVMV, the cassava vein mosaic virus promoter; GFP, green fluorescent protein; 35T, the cauliflower mosaic virus 35S terminator; NosP and NosT, the nopaline synthase gene promoter and its terminator; NptII, the coding sequence of neomycin phosphotransferase II. HA: Hemagglutinin tag. (**B**) Phenotypic comparison of empty vector (EV) and *CsGPX4* overexpression (OX-CsGPX4) *C. sinensis* plants. The picture was taken 1 year after planting in soil. (**C**) Immunoblot detection of HA-tagged CsGPX4 using an anti-HA antibody. Rubisco was used as a loading control. (**D**) Reverse transcription PCR confirmation of *CsGPX4* transgene expression in the OX-CsGPX4 lines. cDNA synthesized from total RNA was amplified using CsGPX4-specific primers. Amplicons of identical size were observed in both OX and EV plant, confirming correct transcript expression. PCR products were resolved by agarose gel electrophoresis.

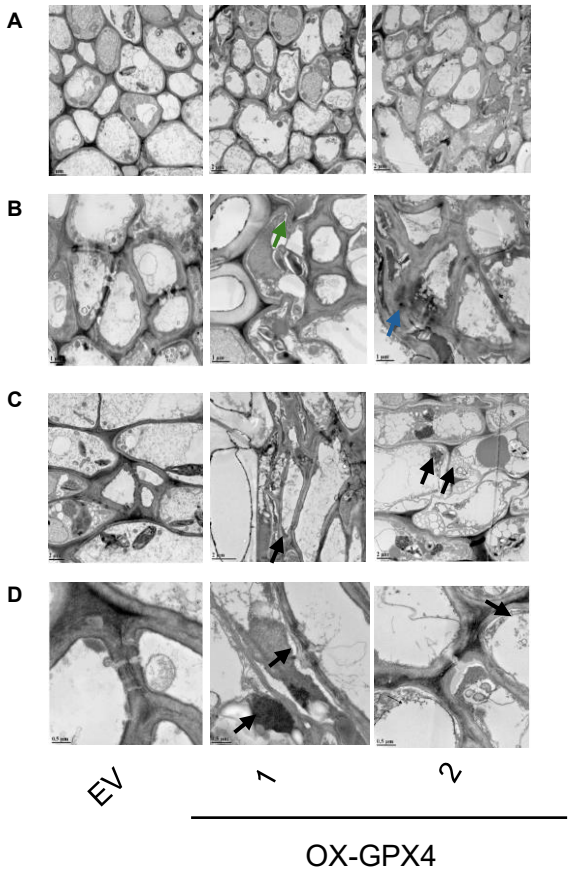

Figure 3. Transmission electron microscopy (TEM) analysis of *C. sinensis* leaves overexpressing *CsGPX4*. (**A**) Overall cell organization. CsGPX4-OX plant cells exhibit irregular boundaries and reduced cytoplasmic density compared to the empty vector (EV) transformed lines. (**B**) Vacuolar structure. CsGPX4-OX cells show pronounced tonoplast (green arrow) and membrane (blue arrow) deformation compared to EV. (**C**) Cytoplasmic organization. CsGPX4-OX cells display extensive vesiculation (arrow) and disorganization of intracellular contents (dashed arrow) compared to EV. (**D**) Membrane integrity. OX lines show fragmented membranes, loss of structural continuity, and accumulation of electron-dense material (arrow), with more severe defects observed in OX-GPX4-2. Scale bars: (**A**) = 2 μm; (**B**) = 1 μm; (**C**) = 2 μm; (**D**) = 0.5 μm.

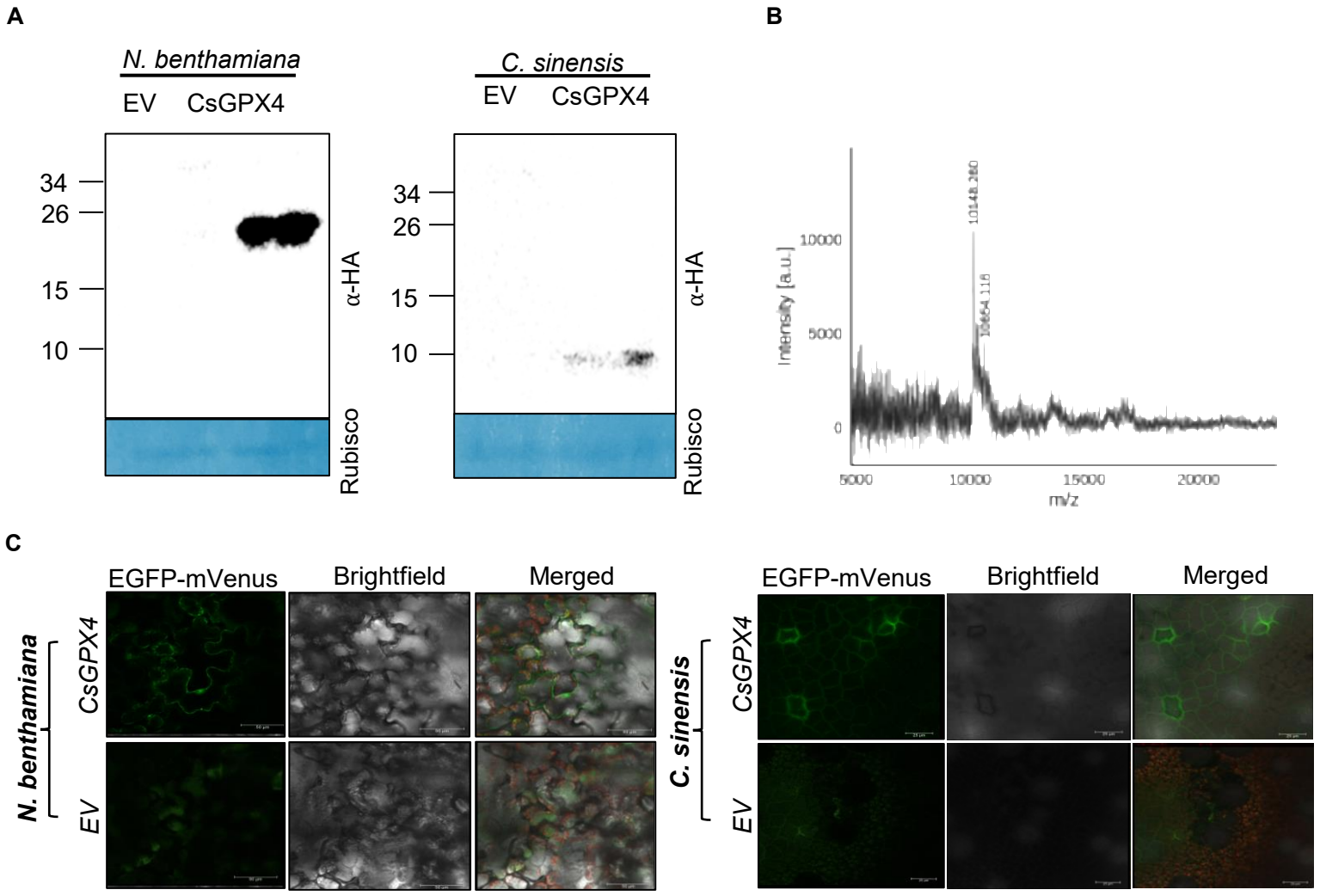

Figure 4. Host specific processing and subcellular localization of CsGPX4 in *C. sinensis* and *N. benthamiana*. (**A**) Immunoblot analysis of CsGPX4-3HA transiently expressed in *C. sinensis* and *N. benthamiana.* A truncated 11 kDa protein was detected in *C. sinensis* and a full-length protein of 22.5 kDa was detected in *N. benthamiana*. Rubisco was used as a loading control. (**B**) MALDI-TOF analysis reveals truncated CsGPX4 proteoform in CsGPX4-OX lines. MALDI-TOF mass spectrum of immunopurified CsGPX4 from citrus leaf tissues expressing HA-tagged CsGPX4 ranging (m/z) 6000-22000. Two prominent peaks were observed at m/z 10,548.260 and 10,654.116. Both masses are substantially lower than the predicted full-length protein (22.5 kDa). The 10,548.260 m/z peak dominates in intensity, suggesting this truncated form is the most stable isoform. Intensity values are presented in arbitrary units (a.u.) scales at x104. (**C**) Subcellular localization of CsGPX4 in *C. sinensis* and *N. benthamiana.* Confocal microscopy of leaf epidermis expressing CsGPX4-EGFP-mVenus. Fluorescence displays a strong membrane-associated pattern in *C. sinensis*. Fluorescence displays GPX4 localization in cytoplasm and nucleus in *N. benthamiana*. Scale bars: *C. sinensis* = 25 µm; *N. benthamiana* = 50 µm.

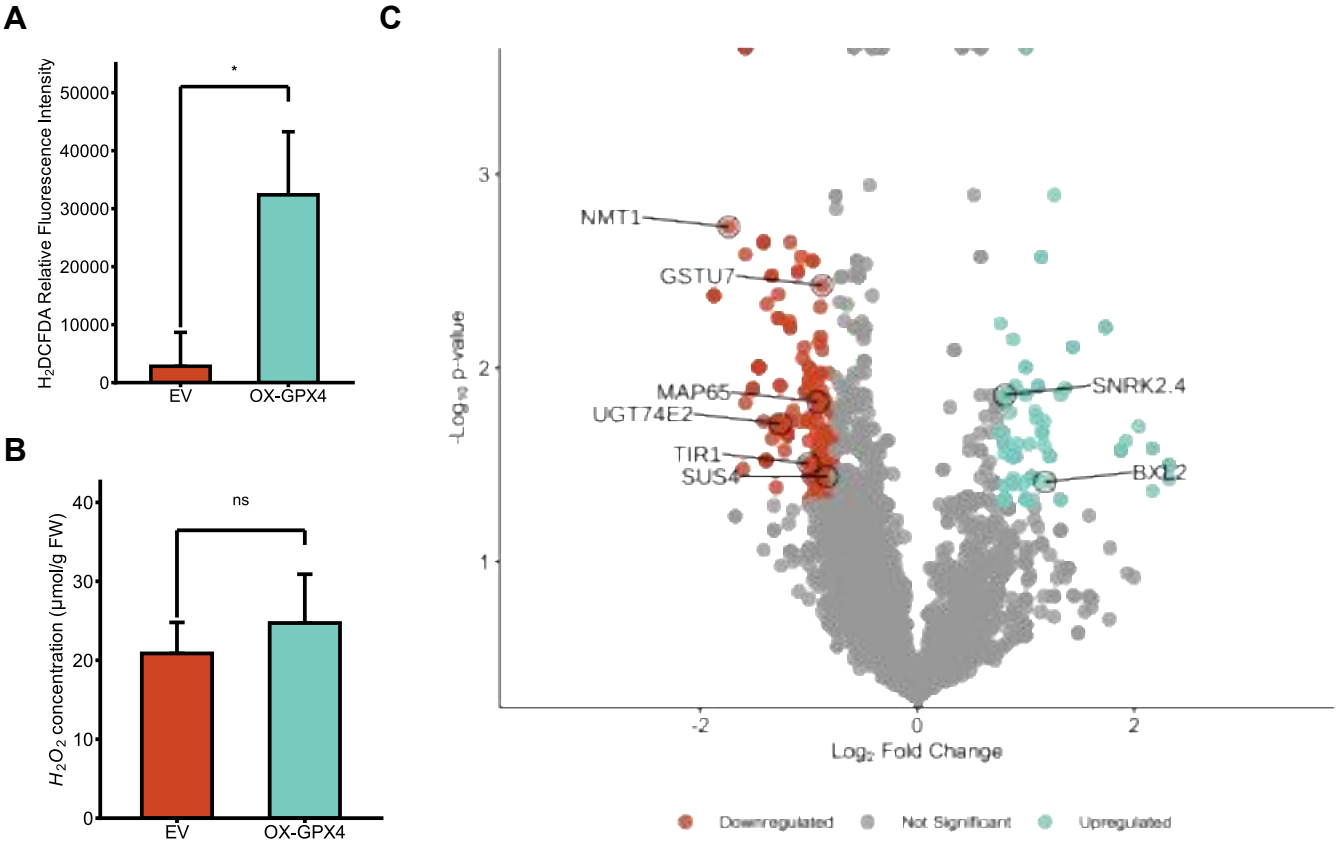

Figure 5. Quantification of ROS levels and proteomic analysis of the CsGPX4-OX lines and wild type. (**A**) Intracellular ROS levels measured using the fluorescent probe H2DCFDA. Three biological replicates were used, $p < 0.05$, student's t test. (**B**) Quantification of extracellular H_2O_2 using the KI assays. Three biological replicates were used, $p < 0.05$, student's t test. (**C**) Volcano plot showing differently expressed proteins in CsGPX4-OX leaves relative to EV controls. Significantly downregulated proteins (red) labeled include NMT1, GSTU7, MAP65, TIR1, UGT74E2, and SUS4. Significantly upregulated proteins (teal) labeled include SnRK2.4 and BXL2. Non-significant proteins (gray). Three biological replicates were used.

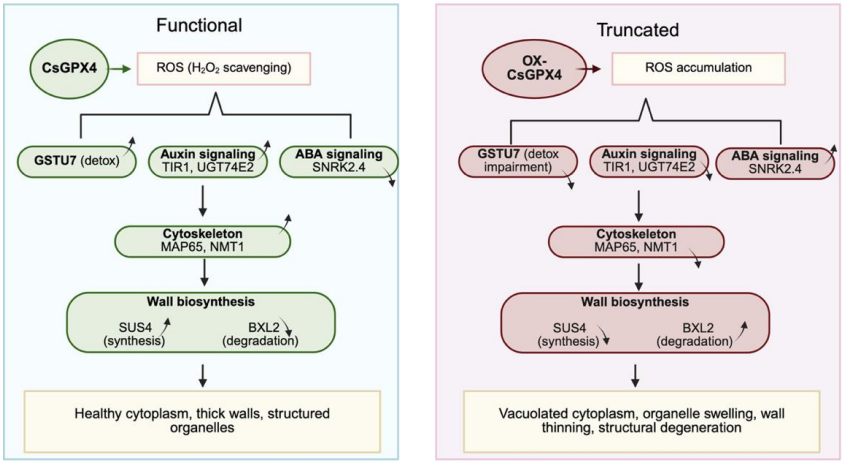

Figure 6. Proposed model of CsGPX4 metabolic shift results of some involved proteins and CsGPX4 truncation affects before and after. Top: Schematic summary illustrating the contrasting roles of CsGPX4 in its functional (left) and truncated (right) states. Functional state (green): Intact CsGPX4 supports reactive oxygen species (ROS) detoxification and redox balance, sustaining cytoskeletal organization (MAP6, NMT1), hormonal signaling (UGT42E, SnRK2.4), and balanced carbohydrate metabolism (SUSA, BXL2). These processes maintain healthy cytoplasmic structure, intact organelles, and thickened cell walls. Truncated state (red): Loss of full-length CsGPX4 compromises peroxidase activity, leading to ROS accumulation and downregulation of redox-related and cytoskeletal proteins (GSTU7, MAP6, NMT1, SUSA). Stress-associated proteins (SnRK2.4, BXL2) become upregulated, promoting vacuolization, organelle swelling, and cell wall degradation.